photonics

Article

Ultracompact Integrated Mode-Order Converter and Reciprocal Optical Diode with Etched Subwavelength Structures

Danfeng Zhu [1,*], Dingnan Deng [1], Junbo Chen [1], Shaobin Qiu [1], Jing Li [2] and Han Ye [2]

[1] School of Physics and Electrical Engineering, Meizhou Intelligent Photoelectric Detection Application Engineering Technology Research Center, Jiaying University, Meizhou 514015, China; deenan@jyu.edu.cn (D.D.); junbochen1991@163.com (J.C.); qshaobin@gmail.com (S.Q.)
[2] State Key Laboratory of Information Photonics and Optical Communications, Beijing University of Posts and Telecommunications, Beijing 100876, China; li_jing@bupt.edu.cn (J.L.); han_ye@bupt.edu.cn (H.Y.)
* Correspondence: zhudanfeng@hotmail.com

Abstract: Three ultracompact integrated photonic devices are proposed, assisted by etched structures. A mode-order converter (MOC) is achieved with a footprint of 0.85 × 1.4 μm^2, which exhibits high performances with insertion loss (IL) below 0.34 dB and mode purity (MP) above 90% within 100 nm waveband. Moreover, a mode blocking filter (MBF) is proposed based on a subwavelength grating with a footprint of 0.8 × 4.12 μm^2, which allows the propagation of TM0 mode but blocks the TM1 mode with a remarkably high extinction ratio of 31.6 dB at the wavelength of 1550 nm. Finally, a compact reciprocal optical diode (ROD) is presented by cascading the abovementioned MOC and MBF with a footprint of 0.85 × 5.9 μm^2. This ROD enables one-way transmissions for both TM0 mode and TM1 mode with contrast ratios of 19.74 dB and 32.04 dB, respectively. The design methodology paves a new way for mode manipulation in integrated multimode photonic circuits.

Keywords: integrated optics; mode manipulation; mode-order converter; subwavelength grating; reciprocal optical diode

Citation: Zhu, D.; Deng, D.; Chen, J.; Qiu, S.; Li, J.; Ye, H. Ultracompact Integrated Mode-Order Converter and Reciprocal Optical Diode with Etched Subwavelength Structures. *Photonics* **2023**, *10*, 563. https://doi.org/10.3390/photonics10050563

Received: 12 April 2023
Revised: 7 May 2023
Accepted: 9 May 2023
Published: 11 May 2023

1. Introduction

Multiplexing technologies have been exploited to address the explosive growth of network traffic in the last decades, based on several physical dimensions of electromagnetic waves, e.g., time, quadrature, wavelength, space, polarization, and mode [1,2]. These multiplexing technologies play a vital role in optical fiber communication systems, especially wavelength-division multiplexing (WDM) [3,4]. In recent years, on-chip optical interconnects featuring high integration, low power consumption, and broad bandwidth have been a research hotspot due to their huge potential application in data centers [5,6]. Multiplexing technologies have enticed significant attention in photonic integrated circuits (PICs) to increase the capacity of on-chip communication networks [7]. It is worth noting that mode-division multiplexing (MDM) utilizes different guide modes as independent channels to load information, offering a new degree of freedom in PICs [8]. MDM is extremely promising owing to its compatibility with WDM and polarization-division multiplexing (PDM) [9,10].

In an MDM system, separate data are encoded on orthogonal spatial eigenmodes and (de)multiplexed in a multimode waveguide. A key component of mode (de)multiplexers is mode converters which enable the free conversion between different spatial eigenmodes. In the past ten years, intensive efforts have been invested in mode-order converters (MOCs) for the implementation of MDM in PICs. Device performances, including broadband, low insertion loss (IL), high mode purity (MP), compact footprints, and outstanding robustness, have been pursued. The operation principles of previous works can be classified into three categories: mode reconstitution, mode coupling, and mode evolution [11]. Manipulating the phase relationship of different eigenmode is the core element for mode reconstitution converters. To achieve this purpose, several strategies have been proposed based on multimode interference (MMI) couplers [12,13], Mach-Zehnder interferometers (MZIs) [14,15], inverse-designed metamaterial waveguides [16,17]. In 1998, J. Leuthold [12] initially demonstrated the conversion between fundamental and first-order modes based on MMI couplers with a mode conversion efficiency (MCE) of 66%. Such MMI-assisted MOCs benefit from broadband and convenient fabrication process but suffer from compromised device size, IL and MP. To solve this issue, in 2006, Y. Huang [14] utilized an MZI coupler to realize a fundamental-to-first order mode converter with a device footprint of 18 × 3 μm^2. The MCE kept above 90% within the waveband from 1450 nm to 1650 nm. This MZI scheme can achieve broadband, low IL, and high MP but except compact footprint. In order to further reduce the device size, in 2012, J. Lu [16] proposed an algorithm-assisted objective-first design method to manipulate eigenmodes of nanophotonic waveguide with high efficiency (~98%) and an ultracompact footprint (1.5–4 square vacuum wavelengths). In the latter years, various algorithms have been explored to improve the design and optimize the process of freeform metamaterial waveguiding for high device performance. Such an inverse-designed method does not rely on physical intuition, and the physical guidelines are not clear. The spatial distribution of materials in the device structure is absolutely free. The inverse-designed method can easily implement some sophisticated functionalities, such as ultracompact and multifunctional devices, which are technical difficulties for the physics-driven forward-design method [18]. However, these subwavelength meta-waveguides are compromised in robustness and require highly accurate fabrication processes, which is a huge challenge for standard silicon fabrication foundries. For the mode coupling category, the converters enable the coupling between different guide modes by utilizing asymmetric directional couplers (ADCs) [19], grating-assisted couplers [20,21], and metasurfaces [22,23] with remarkably low IL and high MP. It is noteworthy that multichannel mode (de)multiplexers can be easily implemented by cascading ADC-based MOCs. The strict phase-matching conditions of ADCs result in a slightly narrow operating bandwidth and a long coupling length. To address these drawbacks, it is extremely efficient to introduce subwavelength gratings (SWGs) into the ADC [24,25]. Another solution is the combination of nanoapertures and L-shaped waveguides [26,27]. In 2020 C. Yao [26] utilized dielectric nanoaperture metasurfaces embedded in an L-shaped silicon waveguide to achieve the fundamental-to-first order mode conversion with an ultrashort coupling length of 2.42 m and MP > 90% within 230 nm bandwidth. For the mode evolution category, the adiabatic transformation of the mode field is the working principle, which means maintaining the conservation of optical wave momentum before and after evolution. In other words, the effective modal indices must be equal or closest. Several schemes have been proposed to implement mode evolution converters, e.g., multichannel branching waveguides [28,29], asymmetric Y-junction [30,31], and tapered waveguides [32]. Such mode evolution strategies can achieve broadband but with several disadvantages, e.g., low MP and long device length. Recently, reconfigurable MOCs have been proposed and demonstrated, assisted by phase change materials (PCMs), which can be applied to multimode photonic convolutional neural networks [33,34]. The functionality of nonvolatile switching offers a new way to photonic computing or advanced reconfigurable circuits for programmable photonic systems [35].

In this paper, three ultracompact integrated photonic devices are proposed, assisted by etched subwavelength structures. Firstly, we demonstrate the mode conversion between the transverse magnetic fundamental mode (TM0) and first-order mode (TM1) with an ultracompact footprint of 0.85 × 1.4 μm^2. This mode-order converter (MOC) is implemented assisted by two parts of high refractive index material (HRIM) embedded in a multimode silicon waveguide with IL = 0.15 dB and MP = 90.7% at the wavelength of 1550 nm. The robustness analyses demonstrate that the IL keeps below 0.2 dB, and MP maintains over 90% within 20 nm deviations of three geometrical parameters and 0.1 variations of the refractive index of HRIM. Secondly, an SWG-assisted mode blocking filter (MBF) is proposed with a compact footprint of 0.8 × 4.12 μm^2, which allows the transmission of TM0 mode but blocks the TM1 mode with an exceedingly high contrast ratio (CR) of 31.6 dB at the wavelength of 1550 nm. This MBF exhibits satisfactory robustness (CR > 28 dB) within 20 nm deviations of two geometrical parameters. Finally, a reciprocal optical diode (ROD) is presented by cascading the proposed MOC and MBF with a compact footprint of 0.85 × 5.9 μm^2. Such ROD achieves the one-way light propagation of both TM0 and TM1 with CR of 19.74 dB and 32.04 dB, respectively.

2. Mode Order Converter

Figure 1a sketches the schematic diagram of the proposed TM-polarized MOC. The functional region is composed of a strip silicon waveguide and HRIM deposited on the silica substrate. A 340 nm thick stripe silicon waveguide is employed to sufficiently support TM-polarized modes [36,37]. HRIM is embedded in an upper and lower silicon waveguide. As is depicted in Figure 1b, the upper HRIM area consists of two symmetric right-angle trapezoids. The lower HRIM area consists of a right triangle and a rectangle. The structural parameters of the proposed MOC are listed in Table 1. In general, the optimized process can be summarized in four steps. The geometry of HRIM is begun with a single rectangle by changing the width and length to achieve higher mode purity. Secondly, another rectangle is added to the functional region. The width and length of each rectangle are swept separately. Thirdly, the upper rectangle is optimized into a pentagon which consists of two symmetric right-angle trapezoids. Finally, the lower rectangle is optimized to a right-angle trapezoid, and the upper right-angle pentagon is moved 50 nm upward to guarantee a higher mode conversion. The footprint of the MOC is ultracompact at 0.85 × 1.4 μm^2.

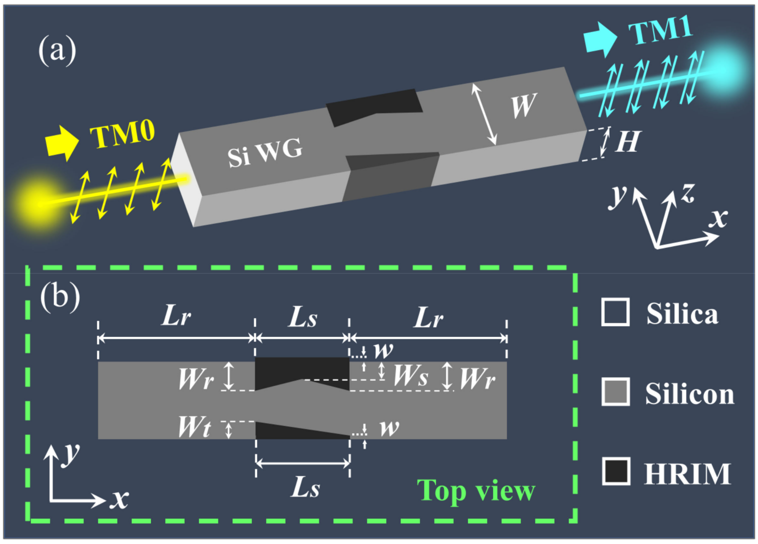

Figure 1. (**a**) Schematic diagram and (**b**) top view of the TM-polarized MOC.

Table 1. Structural Parameters of the TM-polarized Mode-order Converter.

TM0-TM1	H	L_r	L_s	W_r	W_s	W_t	W	w
Value (nm)	340	3000	1400	250	190	160	800	50

The three-dimensional finite-difference time-domain (3D FDTD) method is utilized to calculate and optimize the device's performance [38]. Perfectly matched layers (PMLs) are employed as boundary conditions in the simulations. The refractive indices of silica, silicon, and HRIM are set as 1.44, sqrt (12), and sqrt (12) + Δn, respectively [39]. SiGe alloy is a candidate for HRIM [40,41]. The operation principle can be described as mode decomposition and reconstitution. In brief, the upper and lower HRIM areas aim to provide two paths and simultaneously introduce the proper phase shifts between them. The top two hybridized modes (HP_1 and HP_2) inspired by the functional region are illustrated in Figure 2a,b. The electric field of HP_1 and HP_2 demonstrate that an incident beam is gradually divided into two parts. Figure 2c depicts the propagation constant β of HP_1 and HP_2. The propagation constant difference $\Delta\beta$ demonstrates the existence of phase shift introduced by the functional region. Parameter $\Delta\beta$ can be fitted by a segmented quadratic polynomial:

$$\Delta\beta = \begin{cases} ax^2+bx+c & 0 < x \leq l/2 \\ rx^2+sx+t & l/2 < x \leq l \end{cases} \tag{1}$$

where a, b, c, r, s, t, and l are respectively -0.206, 0.608, 1.51, -0.865, 3.11, 7.15×10^{-2}, and 1.4. The total phase shift is integrated as π at the wavelength of 1550 nm, which enables the mode conversion between TM0 and TM1 for the proposed MOC.

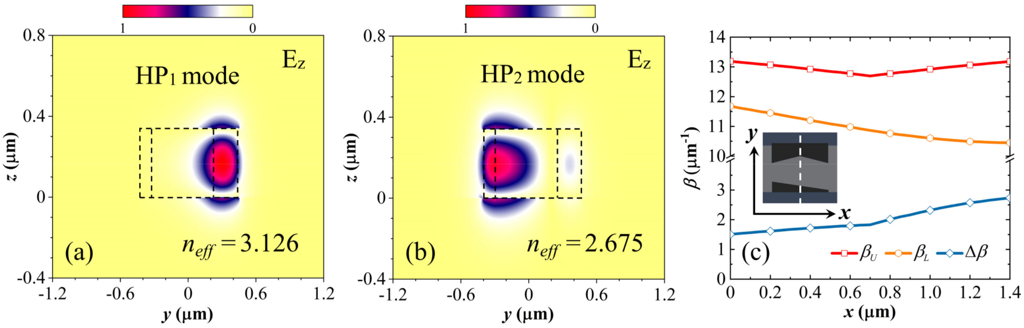

Figure 2. (**a**,**b**) are the top two hybridized modes (HP_1 and HP_2) located at the upper and lower HRIM regions in the middle (x = 0.7) of the functional region. (**c**) Propagation constants β and difference $\Delta\beta$ of HP_1 and HP_2.

Figure 3 depicts the electric field E_Z in the XY plane at the wavelength of 1550 nm. As illustrated in Figure 3a, the TM0 mode is incident at the left port (defined as forward direction), and part of the mode profile focuses on the upper HRIM area while the remaining concentrates in the middle silicon and lower HRIM areas. As mentioned above, these two parts of mode profiles will go out of phase and generate the propagation constants difference. After they propagate through the functional region, the total phase shift is approximately π. The insertion loss (IL) and mode purity (MP) are separately defined as:

$$\mathrm{IL} = -10 * \log_{10} T_{total}\ (\mathrm{dB}) \tag{2}$$

$$\mathrm{MP} = \frac{T_{TMi}}{T_{total}} \times 100\%\ (i = 0, 1) \tag{3}$$

where T_{total} denotes the total output transmittance, and T_{TMi} denotes the output transmittance of the targeted TMi mode. It is convenient to calculate the transmittances of each mode utilizing a mode expansion solver [42]. The TM0 mode is converted to the TM1 mode with IL = 0.15 dB and MP = 90.7%. Due to the reciprocity of the proposed MOC, when the TM1 mode is incident in the backward direction, as shown in Figure 3b, the proposed structure will convert the TM1 mode to the TM0 mode with IL = 0.34 dB and MP = 95.1%. It is worth noting that the footprint is as small as 0.85×1.4 μm^2. As is well known, the inverse-designed metamaterial methods can remarkably reduce the coupling length, thus attaining an ultracompact MOC. To the best of our knowledge, this proposed MOC is comparable or superior to those state-of-the-art works in terms of the device footprint. Such ultracompact MOC could contribute to the high-density integration of PICs.

The spectrum responses of IL and MP are depicted in Figure 4, with bandwidths from 1500 nm to 1600 nm. When the TM0 mode is excited at the left port, the insertion loss maintains below 0.26 dB at the wavelength of 1600 nm and above 0.1 dB at the wavelength of 1500 nm, as shown in Figure 4a. It can be seen in that Figure 4b that the mode purity of targeted TM1 mode presents a peak of 92.1% at the wavelength of 1573 nm and a valley of 89.5% at the wavelength of 1526 nm. Figure 4c illustrates the electric field (E_Z) profile at the right output port, where the TM1 mode is absolutely dominant. As illustrated in Figure 4d,e, when the TM1 mode is inversely incident, the insertion loss shows a peak of 0.34 dB at the wavelength of 1549 nm and a valley of 0.21 dB at the wavelength of 1580 nm. The mode purity of the targeted TM1 mode keeps above 91.8% at the wavelength of 1600 nm and below 95.5% at the wavelength of 1558 nm. It can be observed in Figure 4f that the TM0 mode is absolutely dominant. Two curves of forward TM0 and inverse TM1 incidence appear slightly shifted because of the imperfection TM0-to-TM1 mode conversion. In addition, the TM1 mode has a larger modal area and more complex spatial distribution than the TM0 mode, leading to higher IL (more scattering in the functional region) and MP with TM1 mode inverse incidence.

The robustness of MOC is investigated with several parameters, including Δn, *Wr*, *Ws*, and *Wt*. As illustrated in Figure 5a–c, Δn ranges from 0.7 to 0.9 with a step of 0.05. The insertion loss is the lowest when Δn equals 0.8, and the mode purity keeps above 86.5%. To guarantee high performances of MOC, geometrical parameters *Wr*, *Ws*, and *Wt* must be correspondingly modified. Both parameters, *Wr* and *Ws*, tend to decrease while parameters *Wt* tends to increase. Figure 5d–f depicts the response of insertion loss with varied geometrical parameters *Wr*, *Ws*, and *Wt*. When these three parameters deviate 20 nm, the insertion loss is maintained below 0.17 dB, 0.17 dB, and 0.19 dB, respectively. It can be observed in Figure 5g–i that the mode purity separately keeps over 90.4%, 90.4%, and 89.1% within 20 nm deviations of *Wr*, *Ws*, and *Wt*. In general, the proposed MOC can hold the functionality and exhibit stable robustness.

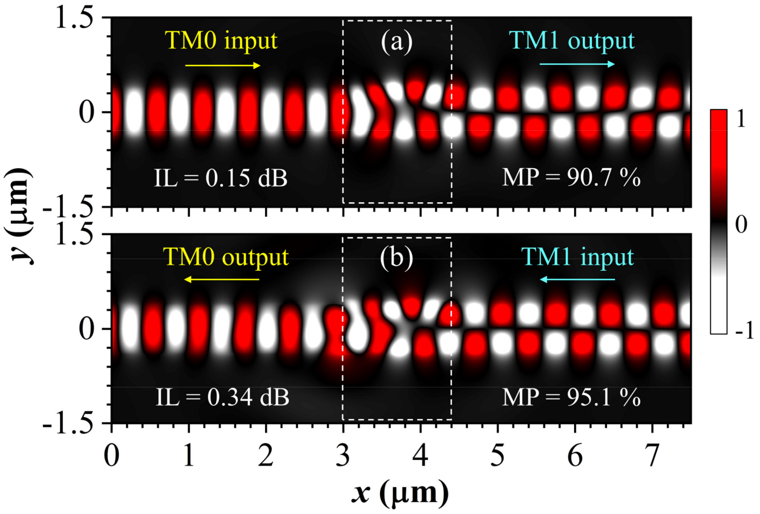

Figure 3. (**a**,**b**) are the electric field (E_Z) profiles with forward TM0 mode and inversely TM1 mode launches, respectively. The rectangular area surrounded by white dotted lines represents the functional region.

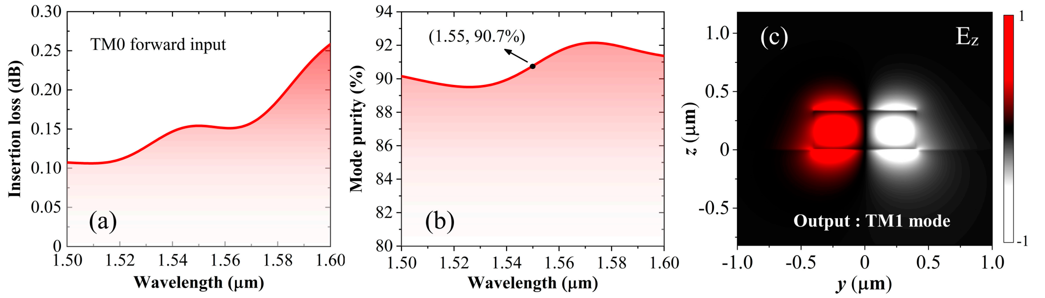

Figure 4. *Cont.*

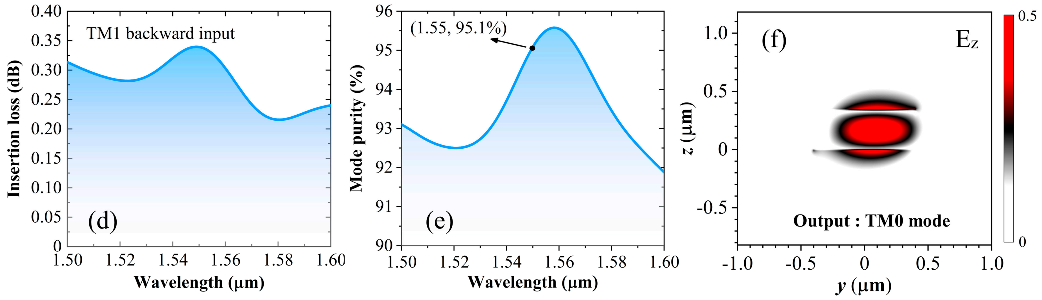

Figure 4. Spectrum responses of (**a**) IL and (**b**) MP, and (**c**) output electric field (E_Z) profile at the right port with TM0 mode forward launch. Spectrum responses of (**d**) IL and (**e**) MP, and (**f**) output electric field (E_Z) profile at the left port with TM1 mode inversely incidence.

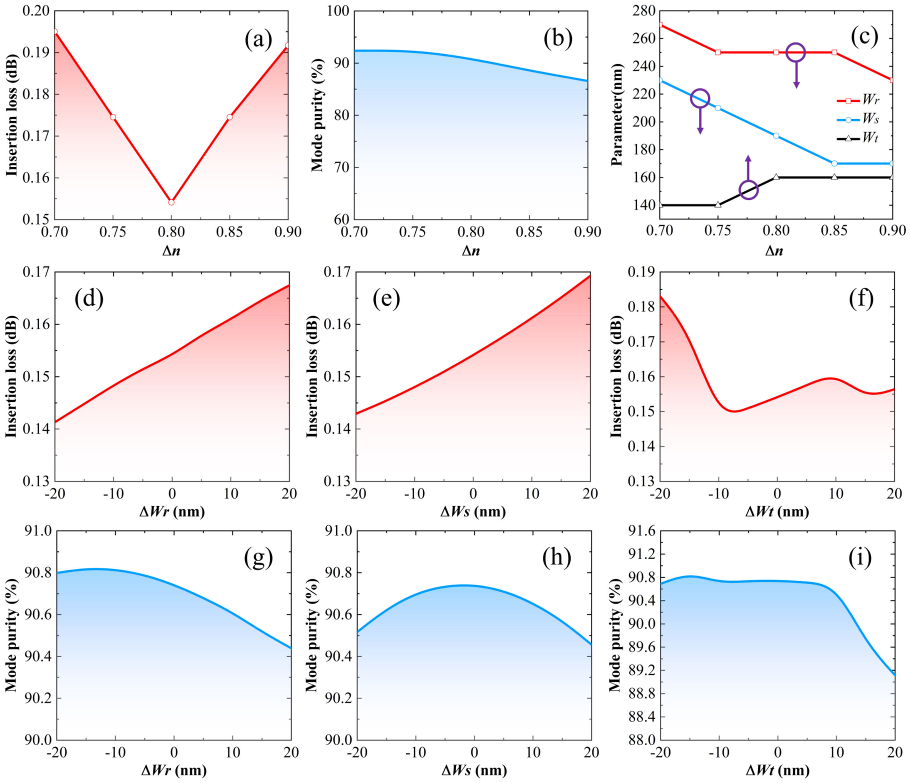

Figure 5. Robustness analysis of the MOC. (**a**) Insertion loss and (**b**) mode purity of varied Δn with (**c**) correspondingly modified geometrical parameters *Wr*, *Ws*, and *Wt*. (**d**–**f**) Insertion loss with varied *Wr*, *Ws*, and *Wt*. (**g**–**i**) Mode purity with varied *Wr*, *Ws*, and *Wt*.

3. Mode Blocking Filter

Subwavelength grating (SWG), consisting of periodic lattices with a period much smaller than the wavelength of signal light, provides new degrees of freedom for the manipulation of effective indices, modal field profiles, mode dispersion, as well as birefringence [43–46]. Mode blocking filters (MBFs) can be implemented in MDM systems, which filter out the undesired modes after demultiplexing different modes. Stripping the fundamental mode can be achieved by grating waveguides [47], Mach–Zehnder interferometer structures [48], asymmetric directional couplers [49], inversed designed metamaterials [50], L-shaped 3D graphene waveguides [51], and so on. It is straightforward to block a higher-order mode due to its weaker confinement through a tapered waveguide with a cut-off width and an appropriate waveguide bend. Both solutions are simple and easy to fabricate but suffer from large device footprints. To address this issue, a SWG-assisted MBF is proposed, as sketched in Figure 6. The pitch of SWG is chosen as 440 nm. The length of the silicon segment is set to 160 nm. The width of the middle silicon bridge is determined as 200 nm. The footprint of the MBF is compact at 0.8 × 4.12 μm^2.

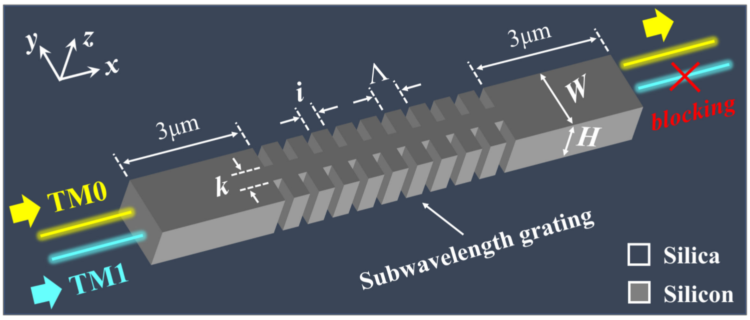

Figure 6. Schematic diagram of the mode blocking filter.

Figure 7a depicts the electric field (E_Z) profile with TM0 mode incidence. The proposed SWG is in the subwavelength regime for the TM0 mode. Therefore, the light propagates through MBF with a low insertion loss of 1.28 dB at the wavelength of 1550 nm. One can find in Figure 7b that the incident light is reflected and radiated. The TM1 mode is blocked with a high insertion loss of 32.88 dB. The extinction ratio exhibits remarkably high with 31.6 dB. The extinction ratio is defined as:

$$\mathrm{ER} = 10 * \log_{10} \frac{T_{TM0}}{T_{TM1}} \ (\mathrm{dB}) \tag{4}$$

where T_{TM0} and T_{TM1} denotes the transmittances of TM0 mode and TM1 mode launches, respectively. Figure 8a,b depict the spectrum responses of insertion loss with TM0 mode and TM1 mode incidences and the extinction ratio. It can be observed that the extinction ratio keeps over 15 dB within a bandwidth from 1500 nm to 1592 nm.

The fabrication tolerance of MBF is investigated with two geometrical parameters, *i* and *k*. As depicted in Figure 9a, the insertion loss for TM0 mode incidence remains below 2.42 dB, and the TM1 mode is blocked with a high insertion loss of over 30.1 dB within a 20 nm deviation of Δ*i*. It can be observed in Figure 9b that the extinction ratio keeps above 28.83 dB. When the geometrical parameter *k* deviates 20 nm, the insertion loss for TM0 mode launch remains below 1.41 dB and over 32.03 dB, as depicted in Figure 9c. The extinction ratio illustrated in Figure 9d keeps above 30.62 dB. One can find that the proposed MBF maintains the functionality within 20 nm fabrication errors, which exhibits satisfactory robustness.

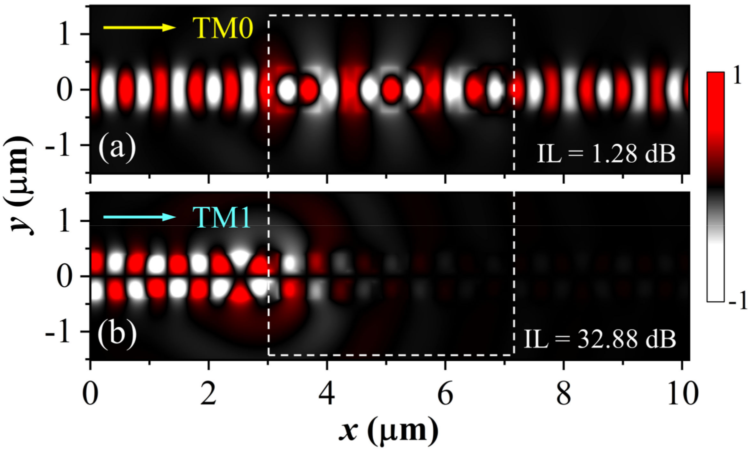

Figure 7. The electric field (E_Z) profiles with (**a**) TM0 mode and (**b**) TM1 mode launches. The white dotted lines refer to the functional region.

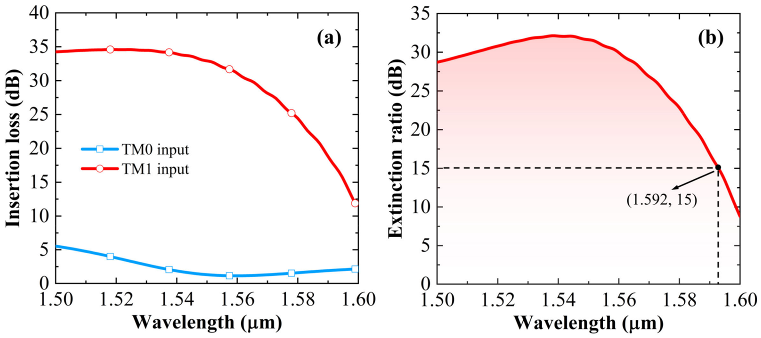

Figure 8. Spectrum responses of (**a**) insertion loss with TM0 mode and TM1 mode incidences and (**b**) extinction ratio.

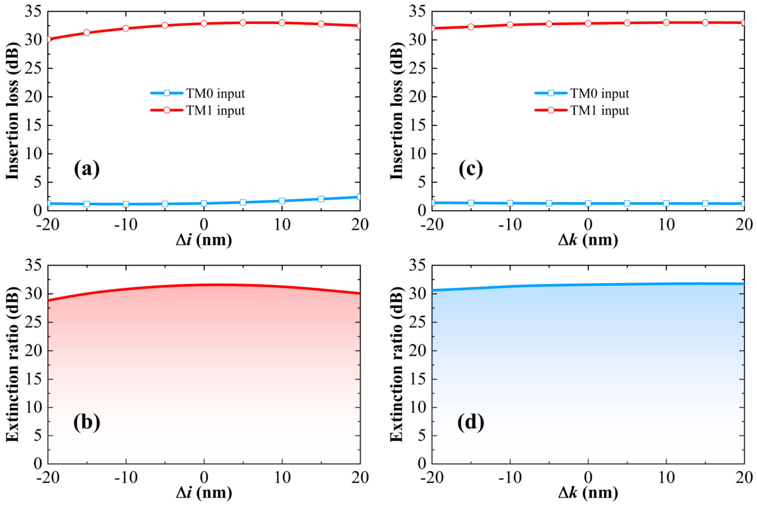

Figure 9. Robustness analyses. The insertion loss with varied geometrical parameters of (**a**) *i* and (**b**) *k*. The extinction ratio with varied (**c**) *i* and (**d**) *k*. The operating wavelength is 1550 nm.

4. Reciprocal Optical Diode

Additionally, an optical diode is another essential building block of PICs. Nonreciprocal optical diodes, typically called optical isolators, completely break the time-reversal symmetry [52] and achieve one-way transmission assisted by magneto-optical materials [53], non-magnetic structures undergoing spatiotemporal modulation [54], and nonlinearity [55]. However, optical isolators are limited in PICs due to the bulky layouts and huge fabrication challenges [56]. To solve these disadvantages, reciprocal optical diodes (RODs) are explored and developed based on passive structures and linear materials, which usually rely on spatial mode symmetry breaking [57,58] and polarization symmetry breaking [59,60]. As depicted in Figure 10a, a ROD is presented by cascading above the proposed mode-order converter and a mode-blocking filter. The functionality is illustrated in Figure 10b. The structural parameters of ROD are listed in Table 2. The footprint of ROD is only 0.85 × 5.9 μm^2.

Table 2. Structural Parameters of the Reciprocal Optical Diode.

Parameter	***i***	***j***	***k***	***l***	***Λ***	***W***	***H***	***N***
Value (nm)	160	380	200	3000	440	800	340	9

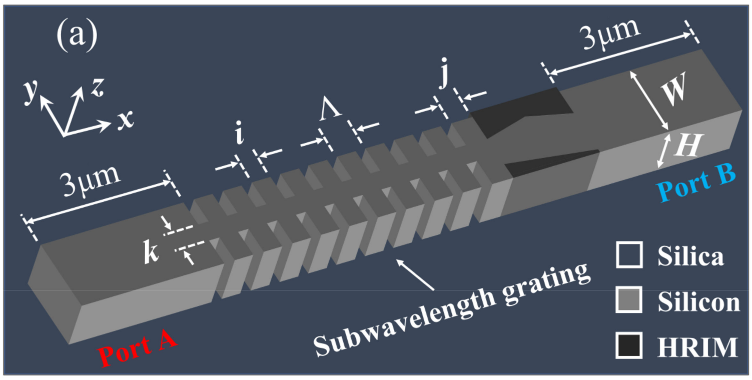

(b)	Port A		Port B	
Input	**TM0**	**TM1**	**TM0**	**TM1**
Output	**TM1**	**Blocking**	**Blocking**	**TM0**

Figure 10. (**a**) Schematic and (**b**) functionality of the reciprocal optical diode.

It is noteworthy in Figure 11 that the present ROD achieves one-way transmission for both TM0 mode and TM1 mode. To the best of our knowledge, most of the previous literature only focused on the fundamental mode. It is convenient to achieve a two-mode ROD by cascading a MOC and an MBF. As depicted in Figure 11a, after the forward incident TM0 mode transmits through the MBF, it is converted to the TM1 mode with a low insertion loss of 1.32 dB. When the TM0 mode is launched inversely, as shown in Figure 11b, it is changed into the TM1 mode, which is blocked by the MBF with a high insertion loss of 21.06 dB. Thus, the asymmetric transmission of TM0 mode is realized with a contrast ratio of 19.74 dB. The contrast ratio is defined as:

$$\mathrm{CR} = 10 * \log_{10}\left|\frac{T_{forward}}{T_{inverse}}\right| (\mathrm{dB}) \tag{5}$$

where $T_{forward}$ and $T_{inverse}$ separately denote transmittances of forward and inversely launches. It can be observed in Figure 11c that the forward incident TM1 mode is blocked by the MBF with an extremely high insertion loss of 33.83 dB. According to the time-reversal symmetry, the inversely incident TM1 mode is converted to the TM0 mode, then propagates through the MBF with a low insertion loss of 1.79 dB. The contrast ratio is remarkably high at 32.04 dB at a wavelength of 1550 nm.

Figure 12a depicts the spectrum responses of insertion loss with TM0 mode and TM1 mode launches. Within the C-band from 1530 nm to 1565 nm, the insertion loss with TM0 mode forward (black dotted curve) and TM1 mode inversely (blue dotted curve) incidences separately keep below 2.67 dB and 3.24 dB. The insertion loss with TM0 mode inversely (orange curve) and TM1 mode forward (red curve) launches keep over 21.07 dB and 30.42 dB, respectively. It can be seen in Figure 12b that the contrast ratio of both TM0 mode and TM1 mode remain above 15 dB within the bandwidth between 1500 nm and 1591 nm. It can be inferred that the contrast ratio difference between the TM0 mode and TM1 mode results from the imperfect mode conversion of the proposed MOC. Additionally, most reported ROD based on spatial mode symmetry breaking only achieve the one-way propagation for the fundamental mode. We innovatively propose a ROD-cascading MOC and MBF, which can enable asymmetrical transmissions for not only TM0 mode but also TM1 mode with a compact footprint of 0.85 × 5.9 μm^2.

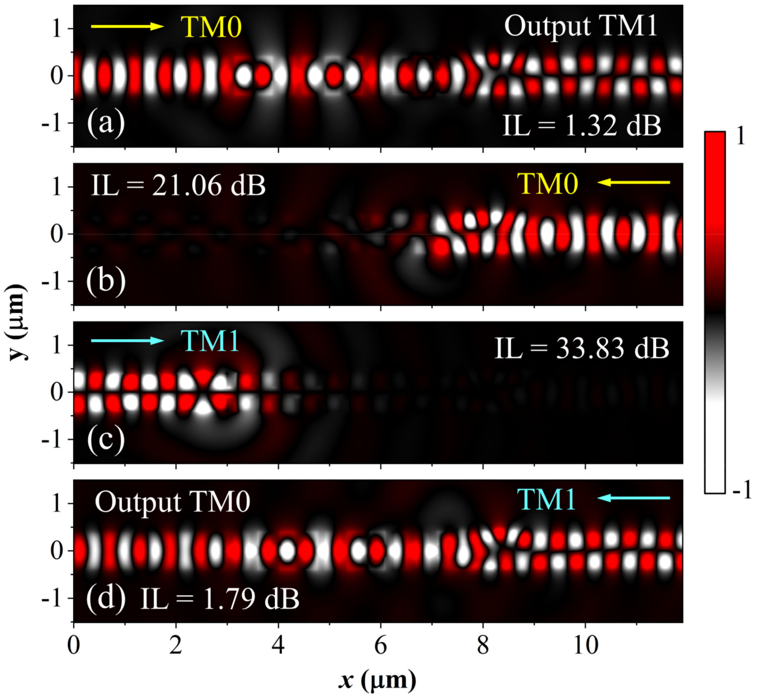

Figure 11. The electric field (E_Z) profiles with (**a**) TM0 mode forward incidence, (**b**) TM0 mode inversely incidence, (**c**) TM1 mode forward launch, and (**d**) TM1 mode inversely launch.

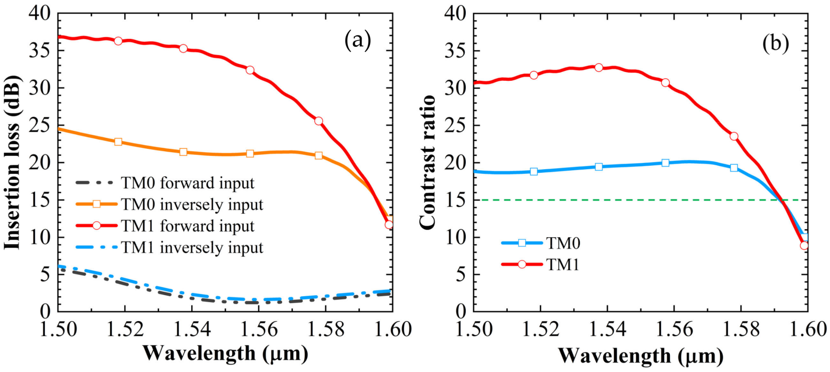

Figure 12. Spectrum responses of (**a**) insertion loss and (**b**) contrast ratio with TM0 mode and TM1 mode incidences.

5. Conclusions

In conclusion, three ultracompact integrated photonic devices are proposed, assisted by etched subwavelength structures, including a mode-order converter, a mode-blocking filter, and a reciprocal optical diode. Firstly, we propose and numerically demonstrate an ultracompact integrated mode-order converter (MOC) with a footprint of 0.85 × 1.4 μm^2. This MOC exhibits a high performance with insertion loss (IL) below 0.34 dB and mode purity (MP) above 90% within bandwidth between 1500 nm and 1600 nm. The fabrication tolerance analysis is investigated in detail, which demonstrates the MOC maintains the functionality (IL < 0.19 dB and MP > 89.1%) within 0.1 of refractive index deviation (Δn) and 20 nm variations of three geometrical parameters (ΔWr, ΔWs and ΔWt). Secondly, a mode blocking filter (MBF) is proposed based on a subwavelength grating (SWG) with a compact footprint of 0.8 × 4.12 μm^2. This SWG-assisted MBF allows the propagation of TM0 mode with a low IL of 1.28 dB but blocks the TM1 mode with an exceedingly high IL of 32.88 dB. The extinction ratio (ER) exhibits remarkably high with 31.6 dB at the wavelength of 1550 nm and keeps over 15 dB within the bandwidth from 1500 nm to 1592 nm. Moreover, the MBF possesses high robustness with ER > 28.83 dB within 20 nm fabrication errors of geometrical parameters (Δi and Δk). Finally, a compact reciprocal optical diode (ROD) is presented by cascading the abovementioned MOC and MBF with a footprint of $0.85 \times 5.9\ \mu m^2$. This ROD enables one-way transmissions for both TM0 mode and TM1 mode with a contrast ratio (CR) of 19.74 dB and 32.04 dB, respectively. The operating bandwidth covers from 1500 nm to 1591 nm with CR > 15 dB. We believe the design methodology can contribute to multimode applications, e.g., mode-division multiplexing.

Author Contributions: Conceptualization, methodology, software, writing—review and editing, D.Z.; validation, D.D.; investigation, J.C.; data curation, S.Q.; visualization, J.L.; supervision, H.Y. All authors have read and agreed to the published version of the manuscript.

Funding: This research was funded by the open competition program of the top 10 critical priorities of Agricultural Science and Technology Innovation for the 14th Five-Year Plan of Guangdong Province (2022SDZG03), Talented Research Start-up Project of Jiaying University (2022RC11), 2023 Science and Technology Project of Jiaying University (2023KJY14), Meizhou City Social Development Science and Technology Plan Project (No. 322E1611).

Institutional Review Board Statement: Not applicable.

Informed Consent Statement: Not applicable.

Data Availability Statement: The data that support the findings of this study are available from the corresponding author upon reasonable request.

Conflicts of Interest: The authors declare no conflict of interest.

References

1. Essiambre, R.J.; Kramer, G.; Winzer, P.J.; Foschini, G.J.; Goebel, B. Capacity Limits of Optical Fiber Networks. *J. Light. Technol.* **2010**, *28*, 662–701. [CrossRef]
2. Tkach, R.W. Scaling Optical Communications for the Next Decade and Beyond. *Bell Labs Tech. J.* **2010**, *14*, 3–9. [CrossRef]
3. Shahpari, A.; Ferreira, R.; Ribeiro, V.; Sousa, A.; Ziaie, S.; Tavares, A.; Vujicic, Z.; Guiomar, F.P.; Reis, J.D.; Pinto, A.N.; et al. Coherent ultra dense wavelength division multiplexing passive optical networks. *Opt. Fiber Technol.* **2015**, *26*, 100–107. [CrossRef]
4. Dittrich, P.; Montemezzani, G.; Günter, P. Tunable optical filter for wavelength division multiplexing using dynamic interband photorefractive gratings. *Opt. Commun.* **2002**, *214*, 363–370. [CrossRef]
5. Miller, D.A.B. Device Requirements for Optical Interconnects to Silicon Chips. *Proc. IEEE* **2009**, *97*, 1166–1185. [CrossRef]
6. Cheng, Q.X.; Bahadori, M.; Glick, M.; Rumley, S.; Bergman, K. Recent advances in optical technologies for data centers: A review. *Optica* **2018**, *5*, 1354–1370. [CrossRef]
7. Kirchain, R.; Kimerling, L. A roadmap for nanophotonics. *Nat. Photonics* **2007**, *1*, 303–305. [CrossRef]
8. Kawaguchi, Y.; Tsutsumi, K. Mode multiplexing and demultiplexing devices using multimode interference couplers. *Electron. Lett.* **2002**, *38*, 1701–1702. [CrossRef]
9. Luo, L.W.; Ophir, N.; Chen, C.P.; Gabrielli, L.H.; Poitras, C.B.; Bergmen, K.; Lipson, M. WDM-compatible mode-division multiplexing on a silicon chip. *Nat. Commun.* **2014**, *5*, 7. [CrossRef]
10. Wang, J.; He, S.L.; Dai, D.X. On-chip silicon 8-channel hybrid (de)multiplexer enabling simultaneous mode-and polarization-division-multiplexing. *Laser Photon. Rev.* **2014**, *8*, L18–L22. [CrossRef]
11. Memon, A.K.; Chen, K.X. Recent advances in mode converters for a mode division multiplex transmission system. *Opto-Electron. Rev.* **2021**, *29*, 13–32.
12. Leuthold, J.; Eckner, J.; Gamper, E.; Besse, P.A.; Melchior, H. Multimode interference couplers for the conversion and combining of zero- and first-order modes. *J. Light. Technol.* **1998**, *16*, 1228–1239. [CrossRef]
13. Uematsu, T.; Ishizaka, Y.; Kawaguchi, Y.; Saitoh, K.; Koshiba, M. Design of a Compact Two-Mode Multi/Demultiplexer Consisting of Multimode Interference Waveguides and a Wavelength-Insensitive Phase Shifter for Mode-Division Multiplexing Transmission. *J. Light. Technol.* **2012**, *30*, 2421–2426. [CrossRef]
14. Huang, Y.Y.; Xu, G.Y.; Ho, S.T. An ultracompact optical mode order converter. *IEEE Photonics Technol. Lett.* **2006**, *18*, 2281–2283. [CrossRef]
15. Perez-Galacho, D.; Marris-Morini, D.; Ortega-Monux, A.; Wanguemert-Perez, J.G.; Vivien, L. Add/Drop Mode-Division Multiplexer Based on a Mach-Zehnder Interferometer and Periodic Waveguides. *IEEE Photonics J.* **2015**, *7*, 7. [CrossRef]
16. Lu, J.; Vuckovic, J. Objective-first design of high-efficiency, small-footprint couplers between arbitrary nanophotonic waveguide modes. *Opt. Express* **2012**, *20*, 7221–7236. [CrossRef]
17. Frellsen, L.F.; Ding, Y.H.; Sigmund, O.; Frandsen, L.H. Topology optimized mode multiplexing in silicon-on-insulator photonic wire waveguides. *Opt. Express* **2016**, *24*, 16866–16873. [CrossRef]
18. Meng, Y.; Chen, Y.; Lu, L.; Ding, Y.; Cusano, A.; Fan, J.A.; Hu, Q.; Wang, K.; Xie, Z.; Liu, Z.; et al. Optical meta-waveguides for integrated photonics and beyond. *Light-Sci. Appl.* **2021**, *10*, 44. [CrossRef]

19. Garcia-Rodriguez, D.; Corral, J.L.; Griol, A.; Llorente, R. Dimensional variation tolerant mode converter/multiplexer fabricated in SOI technology for two-mode transmission at 1550 nm. *Opt. Lett.* **2017**, *42*, 1221–1224. [CrossRef]
20. Jin, W.; Chiang, K.S. Mode converters based on cascaded long-period waveguide gratings. *Opt. Lett.* **2016**, *41*, 3130–3133. [CrossRef]
21. Xiao, R.L.; Shi, Y.C.; Li, J.; Dai, P.; Zhao, Y.; Li, L.Y.; Lu, J.; Chen, X.F. On-chip mode converter based on two cascaded Bragg gratings. *Opt. Express* **2019**, *27*, 1941–1957. [CrossRef]
22. Li, Z.Y.; Kim, M.H.; Wang, C.; Han, Z.H.; Shrestha, S.; Overvig, A.C.; Lu, M.; Stein, A.; Agarwal, A.M.; Loncar, M.; et al. Controlling propagation and coupling of waveguide modes using phase-gradient metasurfaces. *Nat. Nanotechnol.* **2017**, *12*, 675–683.
23. Wang, H.W.; Zhang, Y.; He, Y.; Zhu, Q.M.; Sun, L.; Su, Y.K. Compact Silicon Waveguide Mode Converter Employing Dielectric Metasurface Structure. *Adv. Opt. Mater.* **2019**, *7*, 6. [CrossRef]
24. He, Y.; Zhang, Y.; Wang, H.W.; Sun, L.; Su, Y.K. Design and experimental demonstration of a silicon multi-dimensional (de)multiplexer for wavelength-, mode- and polarization-division (de)multiplexing. *Opt. Lett.* **2020**, *45*, 2846–2849. [CrossRef] [PubMed]
25. Zhu, D.F.; Ye, H.; Liu, Y.M.; Li, J.; Wang, Y.R.; Yu, Z.Y. Silicon subwavelength grating-assisted asymmetric directional coupler around 2 mu m and its applications. *Opt. Laser Technol.* **2021**, *136*, 10. [CrossRef]
26. Yao, C.N.; Wang, Y.L.; Zhang, J.H.; Zhang, X.L.; Zhao, C.; Wang, B.; Singh, S.C.; Guo, C.L. Dielectric Nanoaperture Metasurfaces in Silicon Waveguides for Efficient and Broadband Mode Conversion with an Ultrasmall Footprint. *Adv. Opt. Mater.* **2020**, *8*, 8. [CrossRef]
27. Zhu, D.F.; Zhang, J.Q.N.; Ye, H.; Yu, Z.Y.; Liu, Y.M. Design of a broadband reciprocal optical diode in multimode silicon waveguide by partial depth etching. *Opt. Commun.* **2018**, *418*, 88–92. [CrossRef]
28. Lee, B.T.; Shin, S.Y. Mode-order converter in a multimode waveguide. *Opt. Lett.* **2003**, *28*, 1660–1662. [CrossRef]
29. Low, A.L.Y.; Yong, Y.S.; You, A.H.; Chien, S.F.; Teo, C.F. A five-order mode converter for multimode waveguide. *IEEE Photonics Technol. Lett.* **2004**, *16*, 1673–1675. [CrossRef]
30. Chen, W.W.; Wang, P.J.; Yang, T.J.; Wang, G.C.; Dai, T.G.; Zhang, Y.W.; Zhou, L.Q.; Jiang, X.Q.; Yang, J.Y. Silicon three-mode (de)multiplexer based on cascaded asymmetric Y junctions. *Opt. Lett.* **2016**, *41*, 2851–2854. [CrossRef]
31. Gao, Y.; Zhang, D.M.; Xu, Y.; Ji, L.T.; Chen, W.; Wang, X.B.; Gao, W.N.; Sun, X.Q. Compact six-mode (de)multiplexer based on cascaded asymmetric Y-junctions with mode rotators. *Opt. Commun.* **2019**, *451*, 41–45. [CrossRef]
32. Dai, D.X.; Mao, M. Mode converter based on an inverse taper for multimode silicon nanophotonic integrated circuits. *Opt. Express* **2015**, *23*, 28376–28388. [CrossRef] [PubMed]
33. Wu, C.M.; Yu, H.S.; Lee, S.; Peng, R.M.; Takeuchi, I.; Li, M. Programmable phase-change metasurfaces on waveguides for multimode photonic convolutional neural network. *Nat. Commun.* **2021**, *12*, 8. [CrossRef] [PubMed]
34. Shastri, B.J.; Tait, A.N.; de Lima, T.F.; Pernice, W.H.P.; Bhaskaran, H.; Wright, C.D.; Prucnal, P.R. Photonics for artificial intelligence and neuromorphic computing. *Nat. Photonics* **2021**, *15*, 102–114. [CrossRef]
35. Parra, J.; Olivares, I.; Brimont, A.; Sanchis, P. Toward Nonvolatile Switching in Silicon Photonic Devices. *Laser Photon. Rev.* **2021**, *15*, 18. [CrossRef]
36. Zhu, D.F.; Wang, X.Y.; Li, J.; Ye, H.; Yu, Z.Y.; Liu, Y.M. Design of nonvolatile and efficient Polarization-Rotating optical switch with phase change material. *Opt. Laser Technol.* **2022**, *151*, 8. [CrossRef]
37. Xu, H.N.; Shi, Y.C. Subwavelength-grating-assisted silicon polarization rotator covering all optical communication bands. *Opt. Express* **2019**, *27*, 5588–5597. [CrossRef]
38. Sullivan, D.M. *Electromagnetic Simulation Using the FDTD Method*; John Wiley & Sons: Hoboken, NJ, USA, 2013.
39. Ye, H.; Wang, D.L.; Yu, Z.Y.; Zhang, J.Q.N.; Chen, Z.H. Ultra-compact broadband mode converter and optical diode based on linear rod-type photonic crystal waveguide. *Opt. Express* **2015**, *23*, 9673–9680. [CrossRef]
40. Claps, R.; Raghunathan, V.; Boyraz, O.; Koonath, P.; Dimitropoulos, D.; Jalali, B. Raman amplification and lasing in SiGe waveguides. *Opt. Express* **2005**, *13*, 2459–2466. [CrossRef]
41. Levinshtein, M.E.; Michael, E.; Rumyantsev, S.L.; Shur, M.S. *Properties of Advanced Semiconductor Materials: GaN, AIN, InN, BN, SiC, SiGe*; John Wiley & Sons: Hoboken, NJ, USA, 2001.
42. Snyder, A.; Love, J. *Optical Waveguide Theory*; Chapman & Hall: London, UK, 1983.
43. Halir, R.; Bock, P.J.; Cheben, P.; Ortega-Moñux, A.; Alonso-Ramos, C.; Schmid, J.H.; Lapointe, J.; Xu, D.; Wangüemert-Pérez, J.G.; Molina-Fernández, Í.; et al. Waveguide sub-wavelength structures: A review of principles and applications. *Laser Photonics Rev.* **2015**, *9*, 25–49. [CrossRef]
44. Brunetti, G.; Marocco, G.; Di Benedetto, A.; Giorgio, A.; Armenise, M.N.; Ciminelli, C. Design of a large bandwidth 2 × 2 interferometric switching cell based on a sub-wavelength grating. *J. Opt.* **2021**, *23*, 085801. [CrossRef]
45. Kazanskiy, N.L.; Butt, M.A.; Khonina, S.N. Silicon photonic devices realized on refractive index engineered subwavelength grating waveguides—A review. *Opt. Laser Technol.* **2021**, *138*, 106863. [CrossRef]
46. Guo, Z.; Xiao, J.; Wu, S. Experimental demonstration of a flexible and high-performance mode-order converter using subwavelength grating metamaterials. *Opt. Express* **2023**, *31*, 10744–10757. [CrossRef]
47. Guan, X.; Ding, Y.; Frandsen, L.H. Ultra-compact broadband higher order-mode pass filter fabricated in a silicon waveguide for multimode photonics. *Opt. Lett.* **2015**, *40*, 3893–3896. [CrossRef]

48. Sun, C.L.; Wu, W.H.; Yu, Y.; Zhang, X.L.; Reed, G.T. Integrated tunable mode filter for a mode-division multiplexing system. *Opt. Lett.* **2018**, *43*, 3658–3661. [CrossRef]
49. Chen, X.F.; Shi, X.D.; Qiu, P.F.; Dai, Z.J.; Yu, Y.; Song, X.X.; Zhang, H.T.; Chen, M.Y.; Ye, Y.X.; Ren, X.D.; et al. Efficient mode converters and filters using asymmetrical directional couplers with subwavelength gratings. *Opt. Lett.* **2022**, *47*, 4600–4603. [CrossRef]
50. You, J.Q.; You, G.Q.; Li, S.Y.; Hou, J.; Yang, C.Y.; Chen, S.P.; Gao, D.S. Ultra-compact and low loss on-chip higher order mode pass filter based on topology optimization. *Appl. Phys. Express* **2020**, *13*, 4. [CrossRef]
51. Huang, Q.D.; Chiang, K.S. Polarization-insensitive ultra-broadband mode filter based on a 3D graphene structure buried in an optical waveguide. *Optica* **2020**, *7*, 744–745. [CrossRef]
52. Wang, D.Y.; Yang, B.; Gao, W.L.; Jia, H.W.; Yang, Q.L.; Chen, X.Y.; Wei, M.G.; Liu, C.X.; Navarro-Cia, M.; Han, J.G.; et al. Photonic Weyl points due to broken time-reversal symmetry in magnetized semiconductor. *Nat. Phys.* **2019**, *15*, 1150–1155. [CrossRef]
53. Portela, G.; Levy, M.; Hernandez-Figueroa, H.E. Novel compact magnetless isolator based on a magneto-optical garnet material. *Opt. Laser Technol.* **2023**, *157*, 7. [CrossRef]
54. Tzuang, L.D.; Fang, K.; Nussenzveig, P.; Fan, S.H.; Lipson, M. Non-reciprocal phase shift induced by an effective magnetic flux for light. *Nat. Photonics* **2014**, *8*, 701–705. [CrossRef]
55. Shi, Y.; Yu, Z.F.; Fan, S.H. Limitations of nonlinear optical isolators due to dynamic reciprocity. *Nat. Photonics* **2015**, *9*, 388–392. [CrossRef]
56. Ma, R.; Reniers, S.; Shoji, Y.Y.; Mizumoto, T.; Williams, K.; Jiao, Y.Q.; van der Tol, J. Integrated polarization-independent optical isolators and circulators on an InP membrane on silicon platform. *Optica* **2021**, *8*, 1654–1661. [CrossRef]
57. Ye, H.; Yu, Z.Y.; Liu, Y.M.; Chen, Z.H. Realization of compact broadband optical diode in linear air-hole photonic crystal waveguide. *Opt. Express* **2016**, *24*, 24592–24599. [CrossRef]
58. Nezhad, V.F.; Haddadpour, A.; Veronis, G. Tunable spatial mode converters and optical diodes for graphene parallel plate waveguides. *Opt. Express* **2016**, *24*, 23883–23897. [CrossRef]
59. Menzel, C.; Helgert, C.; Rockstuhl, C.; Kley, E.B.; Tunnermann, A.; Pertsch, T.; Lederer, F. Asymmetric Transmission of Linearly Polarized Light at Optical Metamaterials. *Phys. Rev. Lett.* **2010**, *104*, 4. [CrossRef]
60. Grady, N.K.; Heyes, J.E.; Chowdhury, D.R.; Zeng, Y.; Reiten, M.T.; Azad, A.K.; Taylor, A.J.; Dalvit, D.A.R.; Chen, H.T. Terahertz Metamaterials for Linear Polarization Conversion and Anomalous Refraction. *Science* **2013**, *340*, 1304–1307. [CrossRef]